Characterization of C-Band Coherent Receiver Front-Ends for Transmission Systems Beyond S-C-L-Band

Robert Emmerich, Carsten Schmidt-Langhorst, Colja Schubert, and Ronald Freund

***Abstract*— The reuse of already deployed single mode fiber is seen as one of the key enablers for cost-efficient capacity upgrades of optical transmission systems. Unlocking the benefits of other transmission bands, to further increase the capacity, can enable optical networks to adapt to highly dynamic traffic patterns. In the here and now, C-band based optical coherent receiver frontends would be a cost-effective solution to support bandwidth division multiplexing without the need for bespoke and expensive per band receiver designs. To investigate a potential use of already existing C-band receivers for multi-band applications, we present a simple and rapid measurement method to characterize the quadrature phase error and the electrical output swing. We experimentally characterize four different commercially available C-band receivers from the upper E- to lower U-band covering 25.4 THz (i.e. 200 nm) of total bandwidth. The obtained results reveal that micro-optics based discrete 90° hybrids and discrete indium phosphide (InP) balanced photodetectors are promising candidates for multi-band systems. While at the same time, the investigated receivers based on photonic integrated circuits in InP suffer from a strong quadrature phase error and a reduced common mode rejection ratio in the wavelength regime below the C-band.**

***Index Terms*— Bandwidth division multiplexing, fiber optics, optical fiber communication, optical receivers, ultra wideband technology, wideband, multi-band.**

I. Introduction

WHILE keeping up with the continuing growth in data traffic demands [1] and avoiding the imminent capacity crunch [2], cost reductions must be addressed to overcome the even more significant cost-per-bit crunch [3]. Therefore, innovative approaches for an efficient and adaptable scaling of transmission capacity, without changing the already deployed and installed fiber plants, is a major concern for operators in the mid-term. In this regard, roadmaps for multi-band (MB) or so-called bandwidth division multiplexing (BDM) systems from O- to U-band (1260-1675 nm) covering 59 THz in bandwidth have gained momentum [3], [4], [5], [6]. While at the same time, the experimental research for single mode fiber is mainly limited to partially filled S-C-L-band systems up to a total bandwidth of 19.8 THz [7], [8], [9], [10], and only recently the first experiments including a coherent reception in the E-band are presented [11], [12]. The mismatch between a full O-U-band system and the current research is partially caused by the unavailability of MB or bespoken per band transponders and hence the inevitable use of wavelength limited C-band components-off-the-shelf. As shown in [8], [13], and [14] transmitters based on lithium niobate ($LiNbO_3$) modulators did not show significant wavelength-dependency from the S- to the U-band (up to 1640 nm) in comparison to indium phosphide (InP) modulators. Thus, $LiNbO_3$ modulators are promising candidates for systems beyond the S-C-L-band. However, broadband characterizations of different commercially available coherent receiver frontends (CRF) are not yet available and hence investigations with simple and rapid measurement methods are required to assess their usability in a MB system. In the here and now, standard C-band based coherent receivers having separate signal and local oscillator (LO) input ports are interesting candidates as cost-efficient building blocks for research on next generation BDM systems.

In this contribution, we experimentally characterize four different commercially available CRFs regarding three performance parameters that, when reviewed together, allow a first and rapid evaluation of the CRF's applicability for MB / BDM laboratory experiments. These are, namely the wavelength dependent electrical output swing (i.e. the output amplitude), the wavelength dependent common mode rejection ratio (CMRR), and the wavelength dependent quadrature error (i.e. the hybrid phase deviation from 90°). The first receiver (see Fig. 1(a)) is an integrated C-band based CRF based on a photonic integrated circuit (PIC) in InP including a multimode interference (MMI) hybrid and eight waveguide-integrated photodetectors (PD). This receiver also includes co-integrated transimpedance amplifiers (TIA) for differential operation up to 25 GHz. The second receiver (Fig. 1(b)), for up to 40 GHz, is based on a similar InP MMI whose outputs, however, feed waveguide-integrated on-chip balanced photodetectors (BPD). The receiver does not include TIAs. The third and fourth receivers (refer to Fig. 1(c)) are based on a discrete setup of micro-optics based (free-space) 90° phase- and polarization-diversity hybrids connected to separate discrete InP BPDs with 70 and 100 GHz of analog bandwidth, respectively. All four investigated receivers are commercially available units which cannot be dismantled for individual tests. We instead present a simple "black-box" characterization method for rapid characterization of the receivers. This is in contrast to complex digital signal processing (DSP) based characterization that require a full optical back-to-back transmission system [14]. For our investigations, only two continuous-wave (CW) external cavity lasers (ECL) with a

Manuscript received 3 July 2023; accepted 31 August 2023. Date of publication 7 September 2023; date of current version 18 September 2023. This work was funded in part by the German Ministry of Education and Research (BMBF) under grant 16KIS1282 in the framework of the CELT-IC-NEXT project AI-NET PROTECT (C2019/3-4) and in part by the European Union's Horizon 2020 Research and Innovation Program under grant 101096909 in the Project FLEX-SCALE. *(Corresponding author: Robert Emmerich.)*

The authors are with the Fraunhofer Institute for Telecommunications, Heinrich-Hertz-Institute, Einsteinufer, 10587 Berlin, Germany (e-mail: robert.emmerich@hhi.fraunhofer.de).

Color versions of one or more figures in this letter are available at https://doi.org/10.1109/LPT.2023.3312697.

Digital Object Identifier 10.1109/LPT.2023.3312697

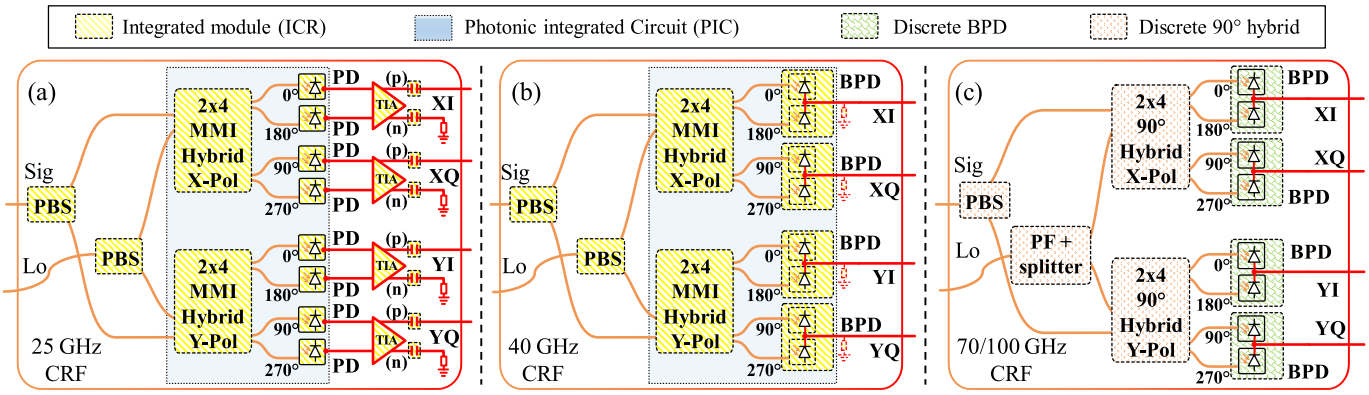

Fig. 1. Block diagram and internal setup of (a) the fully integrated 25 GHz CRF with PDs and TIAs with differential outputs, (b) the fully integrated 40 GHz CRF without TIAs and integrated BPDs for single ended outputs, (c) the discrete 70/100 GHz CRF with discrete (external) BPDs with single ended outputs. Sig: Signal. LO: Local Oscillator. PBS: Polarization Beam Splitter. PF: Polarization Filter.

tuning range of 200 nm (1440-1640 nm), a low speed real time oscilloscope (RTO) and simple digital post-processing (calculating sine-fits) are needed to cover a range of 25.4 THz from the higher E- to the lower U-band. With this setup, all measurements are performed independent of an ultra-wideband (UWB) transmitter or the need for any optical MB amplifiers. The results shown here are representative for usage of the investigated receivers beyond the S-C-L-band (i.e. 1460 – 1625 nm). This measurement concept could also be applied to characterize CRFs based on other technologies like e.g. silicon photonic receivers [15].

II. Experimental Setup

The experimental setup used for the characterization of the four different investigated commercially available coherent receiver frontends, as depicted in Fig. 1(a-c), is shown in Fig. 2.

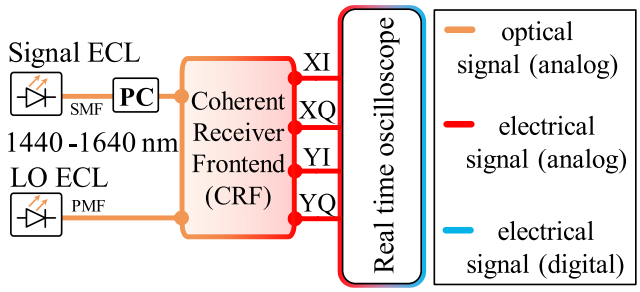

Fig. 2. Experimental setup used for quadrature phase error and output amplitude characterization of the four investigated CRFs over 200 nm. PMF: Polarization Maintaining Fiber, PC: polarization controller.

The ECL for the LO was operated at a fixed output power of +12 dBm for all wavelengths and CRFs. At the beginning of each measurement, the signal (Sig) input port polarization was coarse-aligned at 1550 nm with a polarization controller (PC) to guarantee an equal power distribution (i.e. a ∼50/50 split) between the two polarization branches of the CRF. For the integrated 25 GHz CRF in Fig. 1(a) the signal input power was additionally attenuated to −7 dBm in order not to saturate the TIAs in the receiver, and the polarization alignment was performed in manual gain control mode (MGC) of the TIAs. For all other receivers, the signal input power was set to +8 dBm (optical power measured over both polarizations). Using an external control script, both ECLs are simultaneously stepped from 1440 – 1640 nm in steps of 1 nm while maintaining an optical frequency difference of about ±1 GHz. In order to mitigate fluctuation in the laser output power at the signal and the LO port each measurement was repeated 10 times and the results are averaged. The created electrical analog beat signals (i.e. sine waves) at the four outputs of the receivers are digitized using a 4-channel RTO with more than suitable bandwidth to capture the ±1 GHz offset frequency. In order to be able to connect all investigated receivers (including the 100 GHz CRF unit having 1-mm RF interfaces) to the same RTO, we used a 10 nominal bit 256 GSa/s RTO with 113 GHz of analog bandwidth for convenience, while a lower speed RTO could have been used with appropriate adapters as well. In case of the 25 GHz CRF with differential TIA outputs, we digitized only the four P-outputs of the TIAs and terminated the unused N-outputs with 50 Ohms, as depicted in the block diagram in Fig. 1(a). Please note, that although digitization of both the P- and N-outputs would improve the TIAs linearity as well as double their electrical output swing, it would not affect the wavelength dependencies of the results presented in this work.

For each CRF unit, the path lengths in front of the RTO were de-skewed to avoid inconsistencies in the measurements. To suppress out of band noise, digital band pass filtering (2 GHz, 4-th order Gaussian) around the captured beating signal was applied after signal acquisition. The frequency offset of the filtered signal (the sine wave) is monitored, and the hybrid deviation is calculated based on a sine-fit of the in-phase (I) and quadrature (Q) component within each polarization. This yields both, the electrical output amplitude (swing) of the I and the Q component for each polarization in Fig. 3 (left axis), as well as the quadrature phase error (i.e. the angle deviation between the I and Q component from 90 degree) per polarization as in Fig. 4. Additionally, the CMRR is calculated based on the photocurrents of each of the 8 PDs per CRF [16] measured every 5 nm and plotted as averaged value (over all quadratures) in Fig. 3(b+c) with black markers (right axis). Since the 25 GHz CRF does not provide photocurrent readings, its CMRR could not be determined. The presented results for all amplitudes in Fig. 3 are smoothed with a three tap moving average filter. To ease the interpretation of Fig. 3(a-c), variations in total CRF responsivity (i.e. photodiode responsivity and differences in insertion loss within the MMIs of the PICs or the discrete micro-optics based 90° hybrids) are removed. Hence, all amplitudes are normalized to the highest value at 1550 nm for each CRF individually to provide a reference for operation in the C-band.

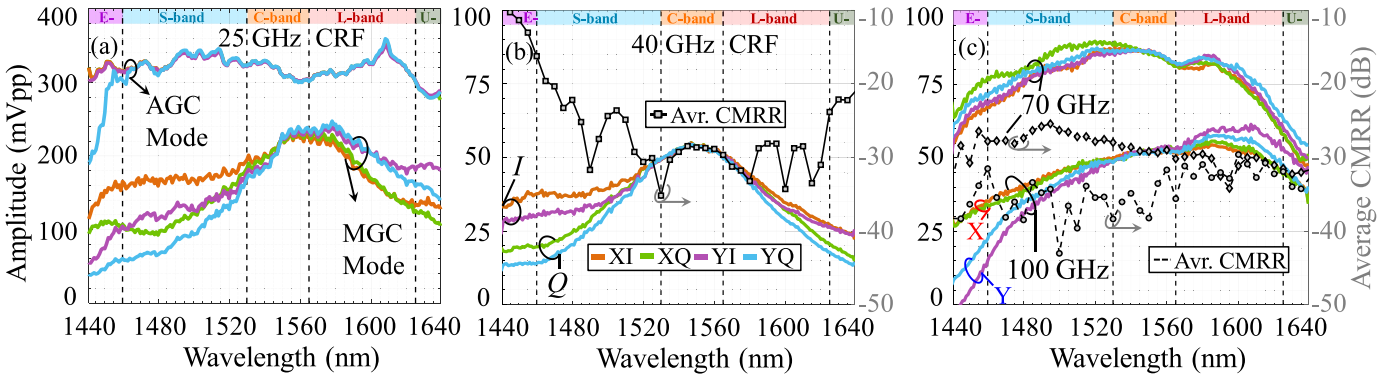

Fig. 3. Output amplitude of (a) the integrated 25 GHz CRF, (b) the integrated 40 GHz CRF and (c) the discrete 70/100 GHz CRF for all four-output components (XI, XQ, YI and YQ) as a function of the wavelength. Additionally, the CMRR (averaged over all components) is included for (b) and (c).

III. Experimental Results and Discussion

Fig. 3(a-c) summarize the measured output amplitudes of the four investigated CRFs for all four outputs, i.e. the X- and Y-polarization (pol) and the I/Q quadratures. In all cases, we are mainly interested in the wavelength dependency rather than the absolute amplitude values, which depend on the TIA gain for the 25 GHz CRF and the optical input power for the other units.

Fig. 3(a) shows a strong wavelength dependency if the integrated 25 GHz CRF is operated in MGC mode (lower set of four curves). In this case, the TIA gain was set to a fixed value in order to achieve an output amplitude of ∼220 mVpp (single ended operation) at 1550 nm. The gain values were kept constant for all investigated wavelengths. Compared to 1550 nm the YQ output amplitude (231 mVpp, blue curve in Fig. 3(a)) of the 25 GHz CRF is e.g. reduced by 84 % at 1440 nm (to 37 mVpp) and by 39 % at 1640 nm (to 139 mVpp). Since such wavelength dependencies are present on all quadratures, the MGC mode is not ideal for MB systems. Additionally, this receiver can be operated in automated gain control (AGC) mode where the TIA gain is automatically adjusted to maintain a constant output amplitude (arbitrarily set to 300 mVpp here). The results for this mode are shown in the upper set of curves in Fig. 3(a), where for nearly all wavelengths within the investigated 200 nm span the set constant output amplitudes are found to be maintained, with minor variations. Only channel YQ (light blue curve) suffers from a drop in output amplitude below 1455 nm. Here the input signal into the TIA was below the acceptable amplitude limit. Note, that automated gain adjustments of TIAs can reduce performance and further investigations are needed. Considering only output amplitude as criterion, AGC mode could enable the 25 GHz CRF to be used for MB systems.

The 40 GHz CRF in Fig. 3(b) follows a very similar amplitude trend vs. wavelength as the 25 GHz CRF in MGC mode, but at a lower total amplitude caused by the absence of TIAs. This is expected since both receiver units are based on a similar MMI design with a strong wavelength dependency. For the C-band this agrees with [17]. Furthermore, a strong grouping of the I and Q quadratures can be observed for shorter and longer wavelengths, introducing an I/Q imbalance. Additionally, the balanced detection (cf. Fig. 1(b)) of the 40 GHz CRF suffered from a strong imbalance in photocurrent on the positive and the negative PD inside all four BPDs. This introduced a DC component with a degradation in the CMRR and makes the 40 GHz CRF unusable for MB applications in the lower S- and U-band.

In case of the results from the 70 GHz CRF shown in the upper sets of curves in Fig. 3(c), the output amplitudes are increased in comparison with the 40 GHz CRF in Fig. 3(b) due to higher responsivity of the BPDs and lower optical loss of the micro-optics based 90° hybrid. Looking at the wavelength dependency, on average, the output amplitude at the ref. wavelength of 1550 nm (87 mVpp) drops by ∼31 % at 1440 nm (to 60 mVpp) and by ∼40 % at 1640 nm (to 52 mVpp). The output amplitudes for all quadratures follow the same wavelength dependency. Since no significant grouping or imbalance in the positive / negative PD currents inside the BPDs are observed, the CMMR remains small and this 70 GHz CRF thus is a promising candidate for multi-band use.

For the discrete 100 GHz CRF shown in the lower sets of curves in Fig. 3(c), a reduced amplitude compared the 70 GHz CRF is observed (due to the lower responsivity of the 100 GHz BPDs). Compared to all other CRFs, a wavelength dependent polarization behavior for wavelengths lower than 1520 nm is present. This results in grouping of the X- and Y-pol as depicted in Fig. 3(c), where the Y-pol experience a stronger loss resulting in a reduced output amplitude. The amplitude at 1440 nm in the Y-pol (light blue line) is reduced by 85 % (to 8 mVpp) while the signal in the X-pol is only reduced by 50 % (to 26 mVpp) compared to 1550 nm (52 mVpp). Since all BPDs in the 100 GHz CRF are from the same type, with a similar wavelength dependent responsivity, we attribute this imbalance to the micro-optics based (free-space) 90° hybrid including the polarization beam splitter, polarization filter and splitter. In order to use this CRF in a MB system, higher optical input power can be used to overcome the additional losses at lower wavelengths.

As a third figure of merit, Fig. 4(a) shows the quadrature phase error between I and Q per polarization for the 25 GHz (lower set of curves) and the 40 GHz CRF (upper set). A strong wavelength dependency below 1500 nm for both integrated receivers is revealed. This is the same in MGC and AGC (plotted) mode for the 25 GHz CRF and thus is attributed to the design of the MMIs inside the PICs. Such observed strong quadrature phase error prevents the usage of these receivers in the lower S-band and E-band, despite the high output amplitudes offered by the 25 GHz CRF in AGC mode. At the same time, the low wavelength dependency of the quadrature error for longer wavelengths and the possibility to operate the 25 GHz CRF in AGC mode indicate a possible

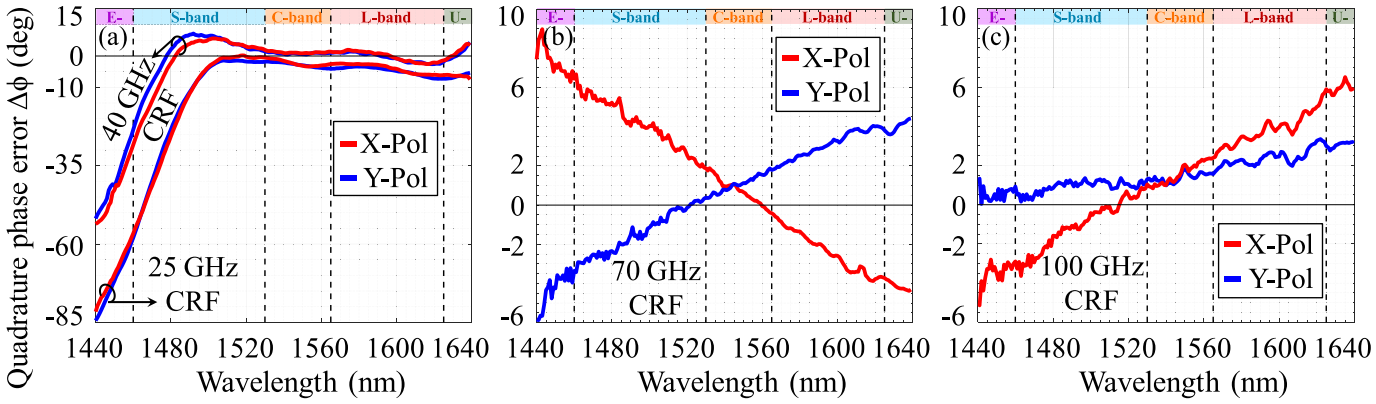

Fig. 4. 90° phase error of (a) integrated 25 and 40 GHz CRF, (b) discrete 70 GHz and (c) discrete 100 GHz CRF for both polarizations as function of wavelength.

applicability from C- to L-band as confirmed in [18]. For the discrete 70 GHz and 100 GHz CRF, the results shown in Fig. 4(b-c) indicate only small deviations of the quadrature phase error versus the wavelength (note the different scale in the y-axes). A measured phase error of ±6° is well within the acceptable range of typical 90° hybrids and can be mitigated by the receiver DSP [14]. The observed different signs of the quadrature phase error slope in Fig. 4(b) are attributed to an "inverted polarization" inside the CRF. Thus, for both discrete setups, operation above or below the C-band is supported as their reduced output amplitude can be overcome by increasing the optical power into the Sig + LO ports of the coherent receivers.

IV. Conclusion

We investigated the feasibility of different C-band based coherent receivers for potential bandwidth division multiplexing systems over 200 nm covering parts of the E- up to parts of the U-band by applying a very simple and rapid measurement method. This can be used as a first step of receiver selections for a multi-band system. Joint characterization of the output amplitude, the CMRR and the quadrature phase error unveiled that these parameters are useful to judge the multi-band capabilities of coherent receivers. Due to their observed strong wavelength dependency, fully integrated InP based standard C-band photonic integrated circuit receivers with multimode interference hybrids are not suitable for operation below 1500 nm. However, discrete receivers showed good CMRR values and small quadrature error over the full investigated wavelength range. With optical input power higher than 12 dBm for the LO and 8 dBm for the Sig port as well as the optional use of additional electrical post-amplification, these receivers are promising candidates for the reception of signals beyond the S-C-L-Band in laboratory experiments.

References

[1] P. J. Winzer and D. T. Neilson, "From scaling disparities to integrated parallelism: A decathlon for a decade," *J. Lightw. Technol.*, vol. 35, no. 5, pp. 1099–1115, Mar. 1, 2017, doi: 10.1109/JLT.2017.2662082.

[2] H. Waldman, "The impending optical network capacity crunch," in *Proc. SBFoton Int. Opt. Photon. Conf. (SBFoton IOPC)*, Oct. 2018, pp. 1–4, doi: 10.1109/SBFoton-IOPC.2018.8610949.

[3] E. Agrell et al., "Roadmap of optical communications," *J. Opt.*, vol. 18, no. 6, pp. 1–40, May 2016, doi: 10.1088/2040-8978/18/6/063002.

[4] J. K. Fischer et al., "Maximizing the capacity of installed optical fiber infrastructure via wideband transmission," in *Proc. 20th Int. Conf. Transparent Opt. Netw. (ICTON)*, Jul. 2018, pp. 1–4, doi: 10.1109/ICTON.2018.8473994.

[5] A. Ferrari et al., "Assessment on the achievable throughput of multi-band ITU-T G.652.D fiber transmission systems," *J. Lightw. Technol.*, vol. 38, no. 16, pp. 4279–4291, Aug. 15, 2020, doi: 10.1109/JLT.2020.2989620.

[6] R. Schmogrow, "Solving for scalability from multi-band to multi-rail core networks," *J. Lightw. Technol.*, vol. 40, no. 11, pp. 3406–3414, Jun. 1, 2022, doi: 10.1109/JLT.2022.3172628.

[7] F. Hamaoka et al., "150.3-Tb/s ultra-wideband (S, C, and L bands) single-mode fibre transmission over 40-km using >519 Gb/s/A PDM-128QAM signals," in *Proc. Eur. Conf. Opt. Commun. (ECOC)*, Sep. 2018, pp. 1–3, Paper Mo4G.1, doi: 10.1109/ECOC.2018.8535140.

[8] R. Emmerich et al., "Enabling S-C-L-band systems with standard C-band modulator and coherent receiver using coherent system identification and nonlinear predistortion," *J. Lightw. Technol.*, vol. 40, no. 5, pp. 1360–1368, Mar. 1, 2022, doi: 10.1109/JLT.2021.3123430.

[9] B. J. Puttnam, R. S. Luís, G. Rademacher, M. Mendez-Astudillio, Y. Awaji, and H. Furukawa, "S-, C- and L-band transmission over a 157 nm bandwidth using doped fiber and distributed Raman amplification," *Opt. Exp.*, vol. 30, no. 6, p. 10011, Mar. 2022, doi: 10.1364/OE.448837.

[10] P. Hazarika et al., "Ultra-wideband discrete Raman amplifier optimization for single-span S-C-L-band coherent transmission systems," *Opt. Lett.*, vol. 47, no. 24, pp. 6472–6475, Dec. 2022, doi: 10.1364/OL.475246.

[11] P. Hazarika et al., "E-, S-, C- and L-band coherent transmission with a multistage discrete Raman amplifier," *Opt. Exp.*, vol. 30, no. 24, pp. 43118–43126, Nov. 2022, doi: 10.1364/OE.474327.

[12] A. Donodin et al., "30-GBaud DP 16-QAM transmission in the E-band enabled by bismuth-doped fiber amplifiers," *Opt. Lett.*, vol. 47, no. 19, pp. 5152–5155, Oct. 2022, doi: 10.1364/OL.468796.

[13] T. Hoshida et al., "Ultrawideband systems and networks: Beyond C + L-band," *Proc. IEEE*, vol. 110, no. 11, pp. 1725–1741, Nov. 2022, doi: 10.1109/JPROC.2022.3202103.

[14] G. D. Rosa et al., "Characterization, monitoring, and mitigation of the I/Q imbalance in standard C-band transceivers in multi-band systems," *J. Lightw. Technol.*, vol. 40, no. 11, pp. 3470–3478, Jun. 1, 2022, doi: 10.1109/JLT.2022.3154888.

[15] C. Doerr et al., "O, E, S, C, and L band silicon photonics coherent modulator/receiver," in *Proc. Opt. Fiber Commun. Conf. Exhib. (OFC)*, 2016, pp. 1–3, Paper Th5C.4, doi: 10.1364/OFC.2016.Th5C.4.

[16] J. E. Johnson, D. R. Stauffer and K. Gass, "Implementation agreement for integrated dual polarization intradyne coherent receivers," Opt. Internetworking Forum, Fremont CA, USA, Tech. Rep. OIF-DPC-RX-01.2, Nov. 2013. [Online]. Available: https://www.oiforum.com/technical-work/implementation-agreements-ias/#Coherent

[17] P. Runge et al., "Monolithic InP receiver chip with a 90° hybrid and 56 GHz balanced photodiodes," *Opt. Exp.*, vol. 20, no. 26, pp. B250–B255, 2012, doi: 10.1364/OE.20.00B250.

[18] R. Emmerich et al., "Capacity limits of C+L metro transport networks exploiting dual-band node architectures," in *Proc. Opt. Fiber Commun. Conf. Exhib. (OFC)*, 2020, pp. 1–3, Paper M2G.5, doi: 10.1364/OFC.2020.M2G.5.